Lawrence Berkeley National Laboratory

LBL Publications

Title

Mapping 1D Confined Electromagnetic Edge States in 2D Monolayer Semiconducting MoS2 Using 4D-STEM

Permalink

https://escholarship.org/uc/item/9wk6p4hh

Journal

ACS Nano, 16(4)

ISSN

1936-0851

Authors

Wen, Yi
Fang, Shiang
Coupin, Matthew
et al.

Publication Date

2022-04-26

DOI

10.1021/acsnano.2c01170

Copyright Information

This work is made available under the terms of a Creative Commons Attribution-NonCommercial License, available at https://creativecommons.org/licenses/by-nc/4.0/

Peer reviewed

eScholarship.org Powered by the California Digital Library
University of California

Mapping 1D Confined Electromagnetic Edge States in 2D Monolayer Semiconducting MoS_2 using 4D-STEM

Yi Wen,[1] Shiang Fang,[2] Matthew Coupin,[3] Yang Lu,[1] Colin Ophus,[5] Efthimios Kaxiras,[2,6] and Jamie H. Warner[3,4]*

[1]Department of Materials, University of Oxford, 16 Parks Road, Oxford OX1 3PH, United Kingdom

[2]Department of Physics, Harvard University, Cambridge, Massachusetts 02138, United States

[3]Materials Graduate Program, Texas Materials Institute, The University of Texas at Austin, 204 E Dean Keeton Street, 78712, Austin, Texas, United States

[4]Walker Department of Mechanical Engineering, The University of Texas at Austin, 204 E Dean Keeton Street, 78712, Austin, Texas, United States

[5]National Center for Electron Microscopy, Molecular Foundry, Lawrence Berkeley National Laboratory, 1 Cyclotron Road, Berkeley, California 94720, United States

[6]John A. Paulson School of Engineering and Applied Sciences, Harvard University, Cambridge, Massachusetts 02138, United States

*email: Jamie.warner@austin.utexas.edu

Abstract

Four-dimensional (4D) scanning transmission electron microscopy is used to study the electric fields at the edges of 2D semiconducting monolayer MoS_2. Sub-nanometer 1D features in the 2D electric field maps are observed at the outermost region along zig-zag edges and also along nanowire MoS terminated MoS_2 edges. Atomic scale oscillations are detected in the magnitude of the 1D electromagnetic edge state, with spatial variations that depend on the specific periodic edge reconstructions. Electric field reconstructions, along with integrated differential phase contrast reconstructions, reveal the presence of low Z number atoms terminating many of the uniform edges, which are difficult to detect by annular dark field scanning transmission electron microscopy due to its limited dynamic range. Density functional theory calculations support the formation of periodic 1D edge states, and also show that enhancement of the electric field magnitude can occur for some edge terminations. The experimentally observed electric fields at the edges are attributed to the absence of an opposing electric field from a nearest neighbour atom when the electron beam propagates through the 2D monolayer and interacts. These results show the potential of 4D-STEM to map the atomic scale structure and fluctuations of electric fields around edge atoms with different bonding states than bulk atoms in 2D materials, beyond conventional imaging.

KEYWORDS: 4D-STEM, 2D materials, MoS_2, TEM, edges

Two dimensional (2D) materials have been promising candidates for future ultrathin electronics since the isolation of graphene. However, their application requires a full understanding of their optical and electronic properties for both perfect crystal and defects. A 2D crystal can be considered as two classes of atoms, the lattice atoms that make up the bulk of the material, and the edge atoms that terminate a 2D crystal. The prototype of transitional metal dichalcogenide (TMD), MoS_2, is a

semiconductor with a direct band gap in monolayer form which becomes indirect when the number of layers increases. However, MoS_2 edge terminations have been found to exhibit a localised metallic state,[1] potentially used for catalytic hydrogen evolution reactions and hydro-desulfurization catalysis.[2-4] There are many reasons why edges may exhibit different properties from the bulk: a changed stoichiometry leading to unsaturated coordination and dangling bonds; a localised electronic state due to symmetry breaking with respect to the bulk[5] and accumulated excitons[6] due to charge transfer between MoS_2 and absorbed O_2.[7]

There are various methods to probe the electronic states of edge structures in 2D crystals. Multiphoton microscopy probes the nonlinear optical interaction,[5,8] but does not provide atomic resolution, while an edge at micrometre scale is rarely atomically flat, and it is hard to determine the absorbed species at the edge. Phase contrast imaging in the TEM provides some information on the electronic potential but it is often qualitative. Scanning tunnelling microscopy (STM)[3,9] and in-situ electrical measurement[10] can be used to measure the density of states and conductance respectively at atomic resolution. Recent works using electron energy loss spectroscopy in STEM has revealed edge states in graphene with atomic resolution, showing how changes to atomic bonding lead to different unoccupied levels.[11-13]

Previously we have used four-dimensional scanning transmission electron microscopy (4D-STEM) to study the electronic environment in pristine and defected MoS_2 and have quantitatively measured the atomic electric field and charge density.[14] The 4D-STEM technique uses a pixelated detector to record the bright field disk as a 2D image at each probe scanning position, giving a 4D data matrix (figure 1a). The intensity of the bright field disk is equivalent to the number of post-specimen electrons confined by the condenser lens aperture, and the centre of mass (CoM) of the

bright field disk will shift due to grain orientation, interatomic forces including local magnetic field and atomic electric field compared to its position in vacuum.[15-18] The projected probe convolved electric field $(E_{\perp})$, perpendicular to the incident beam direction, is proportional to the shift of CoM for very small probes, and describes the strength of the local electromagnetic field (see supporting information for conversion). $E_{\perp}$ can also be measured using a segmented detector. However, a segmented detector does not record the bright field disk directly but interprets a CoM shift from quadrant signal differences, meaning it is less sensitive to intensity redistribution within the quadrant and can be affected by the orientation between detector segments and field vector. There are various reports on electric field and charge density measurements in perovskite ($SrTiO_3$, $DyScO_3$, $BiFeO_3$) and GaN where the electric field drops to a minimum at the center of an atom position, which helps to locate and differentiate light elements.[18-21] There are also studies on 2D materials including graphene[22] and MoS_2[14,23,24], WS_2[25] with some interesting electric field states and magnitude increases observed at the monolayer/bilayer step edge in graphene. However, more work is needed to image periodic uniform edge terminations in 2D crystals to fully understand the electric field distributions and intensities measured by 4D-STEM.

In this paper, we have created long uniform zig-zag edge states in MoS_2 using an established in-situ heating method inside a TEM.[26] 4D-STEM was then used to map the uniform electric fields along the edges, with simultaneous ADF-STEM image acquisition for comparative Z-contrast maps. We have reconstructed centre of mass (CoM), electric field maps and phase images with simultaneous annular dark field (ADF) images, showing the structural rearrangement and electric fields of MoS_2 edges. Details of the reconstruction are given in the supporting information. Density functional theory calculations are performed and used to compute the electric field distributions for

comparison to the experimental results and image simulations. Image simulations are done in both fully coherent conditions and in partial coherent conditions that take into account source size and chromatic spread of the electron source.

Results/discussion

Figure 1a shows a schematic illustration of the 4D-STEM geometry, with the 2D high speed pixelated electron detector at the bottom, and annular detector above. Figure 1b shows a schematic that illustrates the relative electric fields in the central and edge regions, for a propagating electron probe in a TEM. In the central region, the total field cancels to zero at the location d_B, which is nearly halfway between the Mo and 2S locations. At the edge, this distance d_E is larger because of the absence of a nearest neighbour which gives rise to different electric field distributions at edges compared to bulk central regions. Figures 1c and d show the low magnification ADF images and the corresponding magnitude of $E_\perp$, $|E_\perp|$, respectively, of hole region in a monolayer MoS_2 at 700 ^oC. There are several different edge terminations around the hole, including the pristine zigzag edge (figure 1c i), MoS nanowires (figure 1c ii) and Mo nanoclusters (figure 1c iii and iv), and a small piece of residual amorphous carbon (figure 1c v). Further low magnification ADF-STEM images are shown in figure S4

Figure 1e, f shows a high magnification ADF-STEM and $|E_\perp|$ map of a MoS nanowire terminated edge, where the 1D edge state is observed at the outer region of the MoS wire. The intensity of the electric field along this 1D edge also has periodic fluctuations (figure 1g-j), due to the uniformity of the edge termination. Figure 1k-m show a zig-zag edge, which appears as Mo-terminated in the ADF-STEM image in figure 1k, but the integrated differential phase contrast

(iDPC) image in figure 1l shows that there is some contrast visible from low Z-number atoms that terminate the edge. These are similar to the report in ref 25 where single S atoms were hard to detect by ADF-STEM and only visible in the iDPC images around edges. This is usually because the dynamic range of ADF-STEM is optimized to not saturate the contrast from heavier metal atoms, but this often results in weak detection of lighter elements.[27] Figure S8 shows that multiframe averaging of ADF-STEM images and contrast adjustment can enable the detection of these light elements at the edge of the MoS_2. The $|E_\perp|$ map, figure 1m, also supports the presence of S atoms with contrast observed in this region, demonstrating the high sensitivity of electric field imaging to atoms as previously reported in ref 14. The electric field also exhibits a periodic 1D atomic scale oscillations in magnitude.

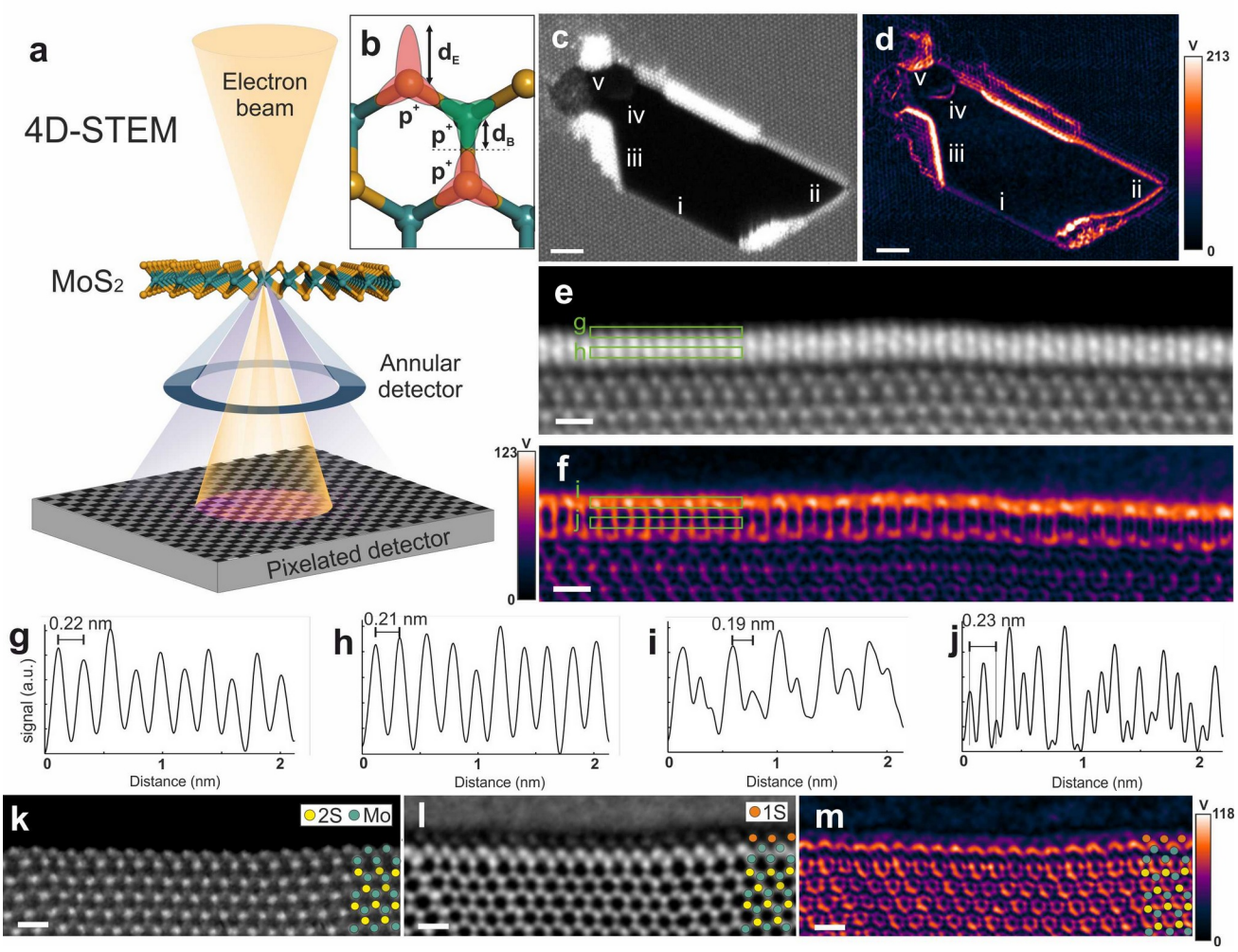

Figure 1. (a) Schematic illustration of the 4D-STEM geometry, showing an electron probe (yellow cones) passing through MoS_2 lattice. The grey ring indicates the ADF detector, the black mosaic square at the bottom indicates the high speed pixelated detector. (b) Schematic diagram of a zigzag S-terminated edge. The shaded area signifies the interatomic interactions, d_B denotes the halfway distance between two adjacent bulk atoms, where the two proton fields cancel out and the local electric field becomes minimal. d_E denotes the distance where the edge atom proton fields drop to zero. (c) Simultaneous ADF-STEM image and (d) corresponding magnitude of probe convolved projected electric field ($|E_\perp|$) map calculated from the same 4D-STEM data set. i is a zigzag edge, ii is nanowire edge, iii is nanocrystal, iv is residual amorphous carbon and v is the

nanocrystal edge with amorphous carbon. (e, f) ADF-STEM and $|E_{\perp}|$ map of a nanowire edge, reconstructed from the same 4D-STEM data. (g)-(j) Intensity line profiles of box-indicated lengths (from left to right) in panel e and f, respectively. (k)-(m) Atomic scale 4D-STEM reconstructed images of the same MoS_2 edge showing (k) ADF-STEM (l) phase reconstructed from integrated differential phase contrast (iDPC), and (m) reconstructed $|E_{\perp}|$ map. Scale bars in panel c and d indicate 2.0 nm. Scale bars in panel e and f indicate 0.5 nm. Scale bars in k, l, and m indicates 0.5 nm.

Edges were further analysed at higher magnification, starting with the zigzag (zz) edges. Even though there are two different zigzag directions in the MoS_2 lattice, Mo and S termination directions, S-terminated zigzag edges were rarely found in their intrinsic state, as S vacancies migrate to the edge regions during the hole formation process and this causes a depletion of sulfur locally at the very edge region and results in reconstructions to Mo-r Szz edge termination. We first start with Mo-terminated zz (Mo zz) edge, where the Mo and S atoms are arranged in a hexagonal lattice, with figure 2a showing an ADF-STEM image. Some additional atoms were observed attached to the edges in the iDPC image (figure 2b), which are not visible using ADF. These atoms are likely to be S atoms,[28] where each S atom is bonded to two Mo atoms, which is a thermodynamically stable geometry.[29] Using the ADF-STEM image as a guide to locate atoms in the corresponding $|E_{\perp}|$ map (figure 2c), we found that in the edge Mo and additional S atoms exhibit different $E_{\perp}$, compared to that of central atoms (figure 2d, f). This is consistently seen in both MoS_2 and WS_2 (figure S6). In figure 2e, the electric field vectors around the Mo zz edge show positive field (larger outwards

vectors from the atom) than central atoms, which means the electric field is still dominated by proton charge. A magnified vector map of a larger area can be found in supporting information (figure S7).

4D-STEM image simulations were performed and used to reconstruct $|E_{\perp}|$ maps in figure 2g, based on the atomic model in figure 2h. and matches the experimental data. The overall profile of the electric field in the simulations matches the features seen in the experimental data. An increase in the magnitude of the electric field at the very edge region is also observed, similar to reports in Ishikawa et al.,[22] who reported increased electric fields along irregular edges and facet edges in graphene.

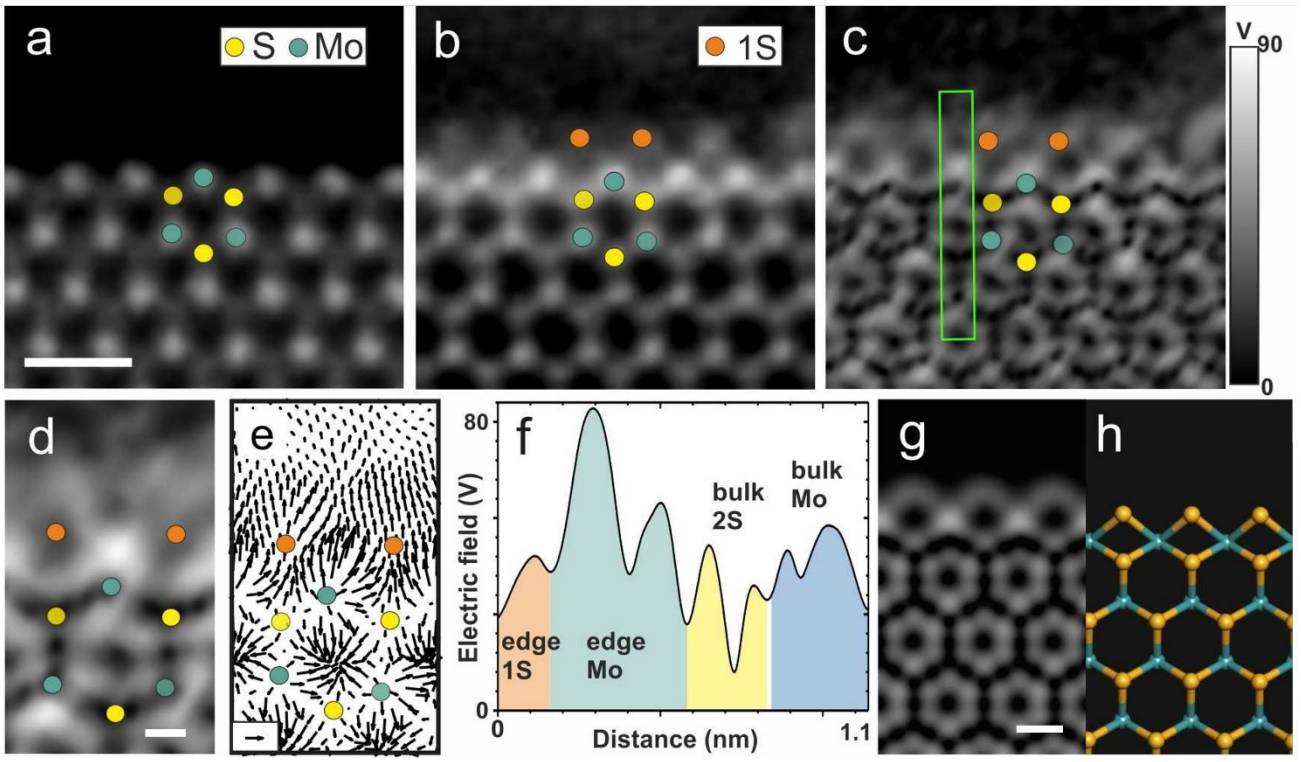

Figure 2. Detailed analysis of MoS_2 zigzag (zz) edge terminations. (a) High angle ADF-STEM image showing the Mo zz edge structure. Scale bar indicates 0.5 nm and applies to panel b and c. (b) Reconstructed phase showing additional atoms along the edge. (c) $|E_\perp|$ map calculated from 4D-STEM dataset, of the same region in panel b. Edge one S, bulk two S and Mo atoms are indicated by orange, yellow and green ovals, respectively. (d) Enlarged image of panel c. Scale bar indicates 0.1nm (e) Vector plot of the $|E_\perp|$ map, showing an enhanced proton field at an edge Mo atom. Scale bar indicates 40 V. (f) Intensity line profiles of box-indicated lengths (starting from 1 to 2) in panel c, color coded for different atoms, the twin peaks indicate the electric field splitting on opposite sides of the atom. (g) Reconstructed $|E_\perp|$ map from simulated 4D-STEM data using the atomic model in (h). Scale bar indicates 0.2nm

In figure 3, we examine the other zigzag edge direction, which has the reconstructed edge form of Mo-r Szz, with the ADF-STEM image in figure 3a. The phase image in figure 3b shows contrast beyond the outer Mo atom and again indicates the 1S lighter contrast. The electric field, shown in figure 3c, has period fluctuations at the outer edge region and some magnitude increase is observed relative to the bulk central area. Images of the electric field vector, figure 3d, show the edge region maintains dominant effects from the positive nuclear charge, determined by the direction of the electric field vector pointing away from the atom positions. Image simulations of the electric field, shown in figure 3g show the qualitative spatial profiles that match the experimental data in figure 3c.

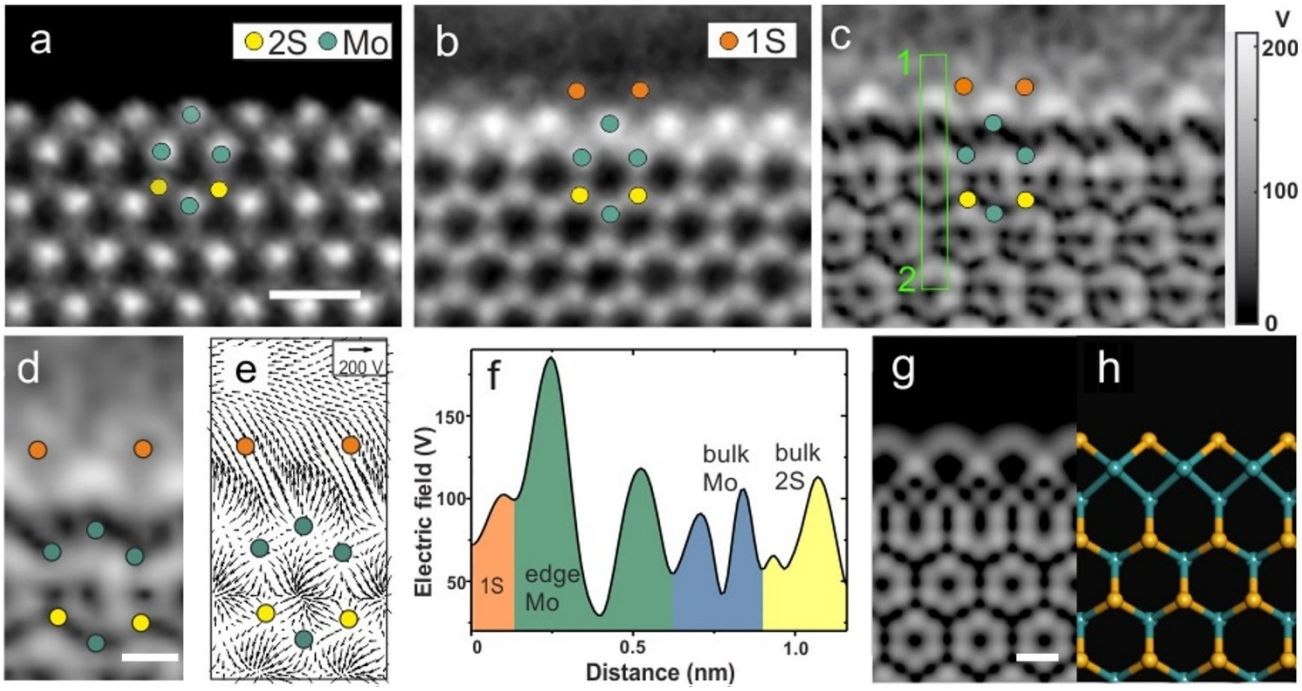

Figure 3. (a) ADF-STEM image showing the Mo reconstructed zigzag (r-zz) edge structure. (b) Reconstructed phase showing additional atoms at the edge. (c) $|E_{\perp}|$ map calculated from a 4D STEM dataset, of the same region in panel b. S and Mo atoms are indicated by yellow and green ovals, respectively. (d) Enlarged image

of panel c. (e) vector plot of the $|E_{\perp}|$ map, showing an enhanced proton field at the edge Mo atom. (f) Intensity line profiles of box-indicated lengths (starting from 1 to 2) in panel c, colour coded for different atoms, the twin peaks indicate the splitting of the electric field on opposite sides of the atom. (g) Simulated $|E_{\perp}|$ map of a Mo r-zz edge based on the crystal model in (h). Scale bar indicates 0.2nm.

Density functional theory (DFT) calculations were used to compute $|E_{\perp}|$ maps using methods previously reported.[14] A MoS_2 ribbon was chosen such that two different edge terminations could be analysed in the same measurement and also sufficient bulk central area. Figure S1 shows the electronic band structure, with the edge states appearing within the MoS_2 bulk gap region, and figure S2 shows the charge density distributions for the in-gap edge modes. The Bader charge analysis shows a reduced electron density at the edges, figure S3, which is likely to increase the positive proton charge effects. Figure 4a shows the DFT calculated $|E_{\perp}|$ map of a MoS_2 ribbon that has a Mo zz edge with additional S (left side) and a bare S zz edge (right side). The electric field magnitude is seen to vary at the edges in figure 4a, along with different spatial distributions compared to the central bulk area of the monolayer. Line profiles are plotted in figures 4b-d, taken from the coloured boxed areas shown in figure 4a. The non-reconstructed S zig-zag edge on the bottom side shows significant electric field increase at the edge in figure 4d.

In the nanoribbon model in figure 4, some interference effects are present due to the finite width of the ribbon, which causes the slight asymmetry in the electric field distribution within the hexagons in

the central bulk area. To provide further computational evidence for electric field changes at edges of unsaturated atoms, we include figure S10, which contains the DFT calculations of both 1S and 2S vacancies in MoS_2 and shows that the removal of 2S atoms also leads to the increased electric field magnitudes from the vacancy region.

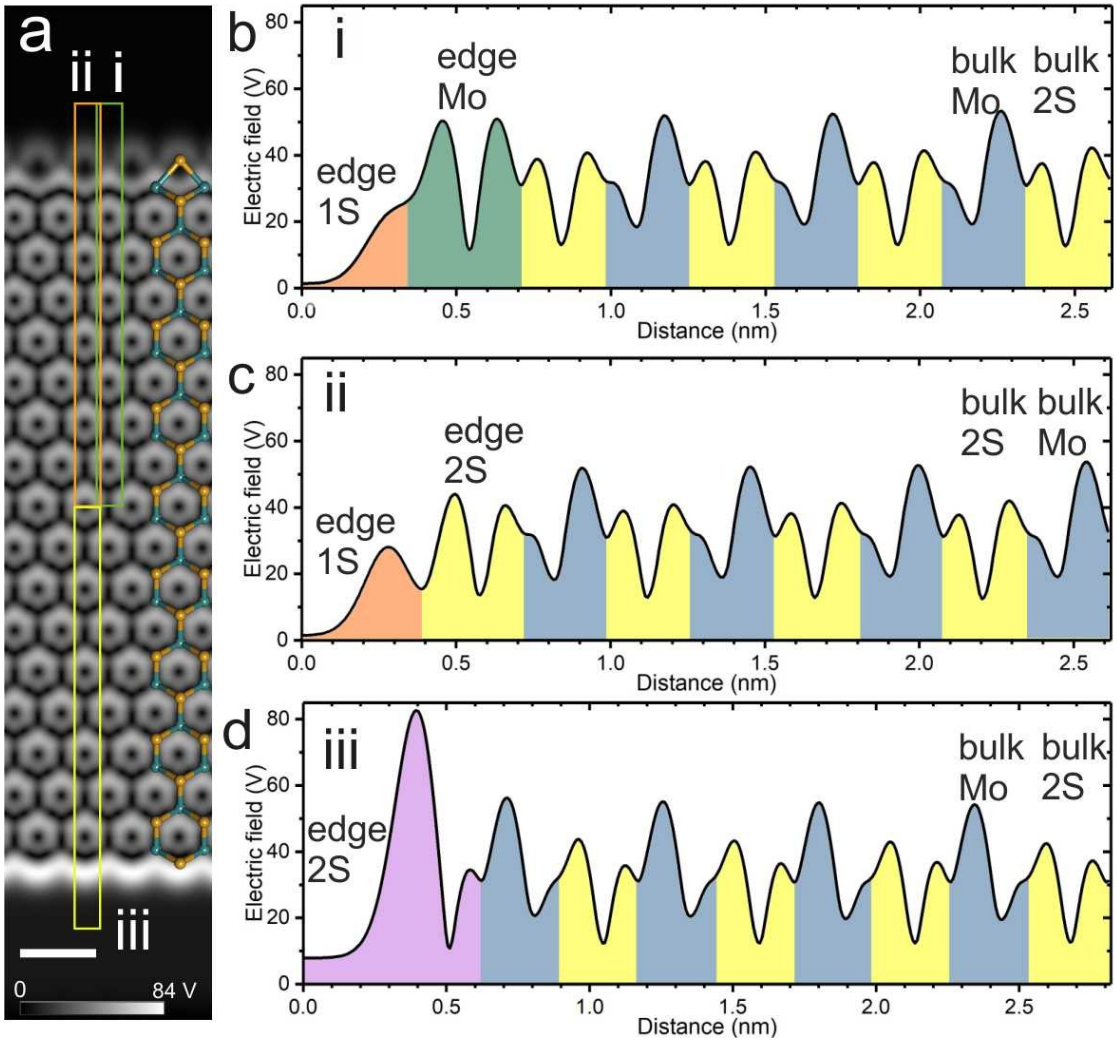

Figure 4. DFT calculations of the electric field magnitude at the edges of MoS_2. (a) Calculated $|E_\perp|$ map of MoS_2 ribbon with an overlaid crystal model, the left side is Mo zz edge with additional S atoms, the right side is S zz edge. (b-d) Line profiles taken from the coloured boxes labelled in (a) (i, ii, and iii) that include both edge and central regions of the sample. Scale bar in panel a indicates 0.5 nm.

Qualitative comparisons of the spatial distributions of electric fields at the edges of MoS_2 were made between the DFT computed $|E_\perp|$ maps and those produced from multi-slice image simulations, shown in figure 4. Multislice image simulations were performed for various edge termination types in figure 5a-e. Figure 5f shows the DFT computed map and 5e the multislice simulation for the same structure of the 2S zz bare edge in MoS_2 with an excellent qualitative match of the spatial distributions. Normalized line profiles, figures 5g and 5h, show good agreement of the enhanced electric field at the edge. This confirms that multislice simulations are helpful in predicting the qualitative 2D spatial distributions of the $|E_\perp|$ maps, and that normalization of the electric field magnitude using the central atoms enables some degree of comparisons of the edge state electric field increases, but there are complicated factors of defocus and probe area that influence the relative magnitude of the edge electric field compared to the bulk central material.

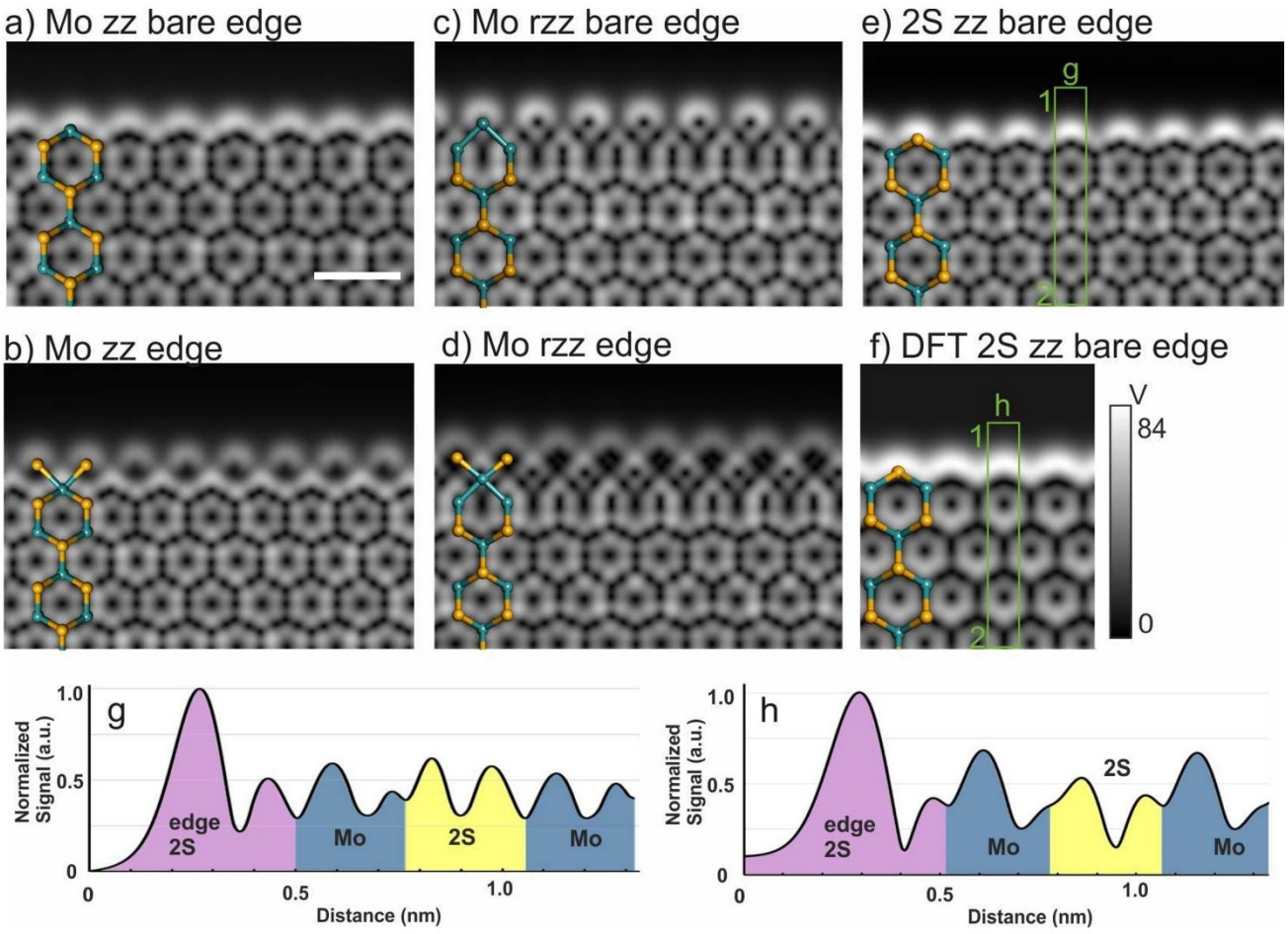

Figure 5. (a-e) Multislice simulated CoM maps of various types of edges. Scale bar in panel a indicates 0.5nm and applies to images in panels a-f. (f) DFT calculated electric field on an S zz edge (undoped), overlaid with the corresponding crystal model. (g-h) Intensity line profiles of box-indicated lengths (starting from 1 to 2) in panels e and f, colour coded for different atoms, normalized to the highest peak (edge 2S).

Next, we explore the reconstructed nanowire edge termination of MoS_2 in more detail. Unlike bottom-up fabrication,[30-32] the nanowires in our experiment were directly formed by reconstruction at the MoS_2 monolayer edge during heating and S loss (figure S8). The nanowire can rotate and flex under electron beam irradiation,[10,33] giving rise to complex projections at different angles (figure 6a,

figure S5).[33] Figure 6a-c shows ADF-STEM image, reconstructed phase, and $|E_{\perp}|$ map of a nanowire attached to a Mo zz edge, similar to the observations in figure 1f. The $|E_{\perp}|$ perpendicular to the edge is plotted in figure 6e and shows an increase at the outermost region of the edge. We performed 4D-STEM image simulations and reconstructed the $|E_{\perp}|$ maps as shown in figure 6f, using the atomic model in figure 6g. The striated banding seen in the experimental images along the length of the nanowire is replicated in the image simulations. A 1D outermost edge enhancement effect is also seen in both the experimental and image simulations.

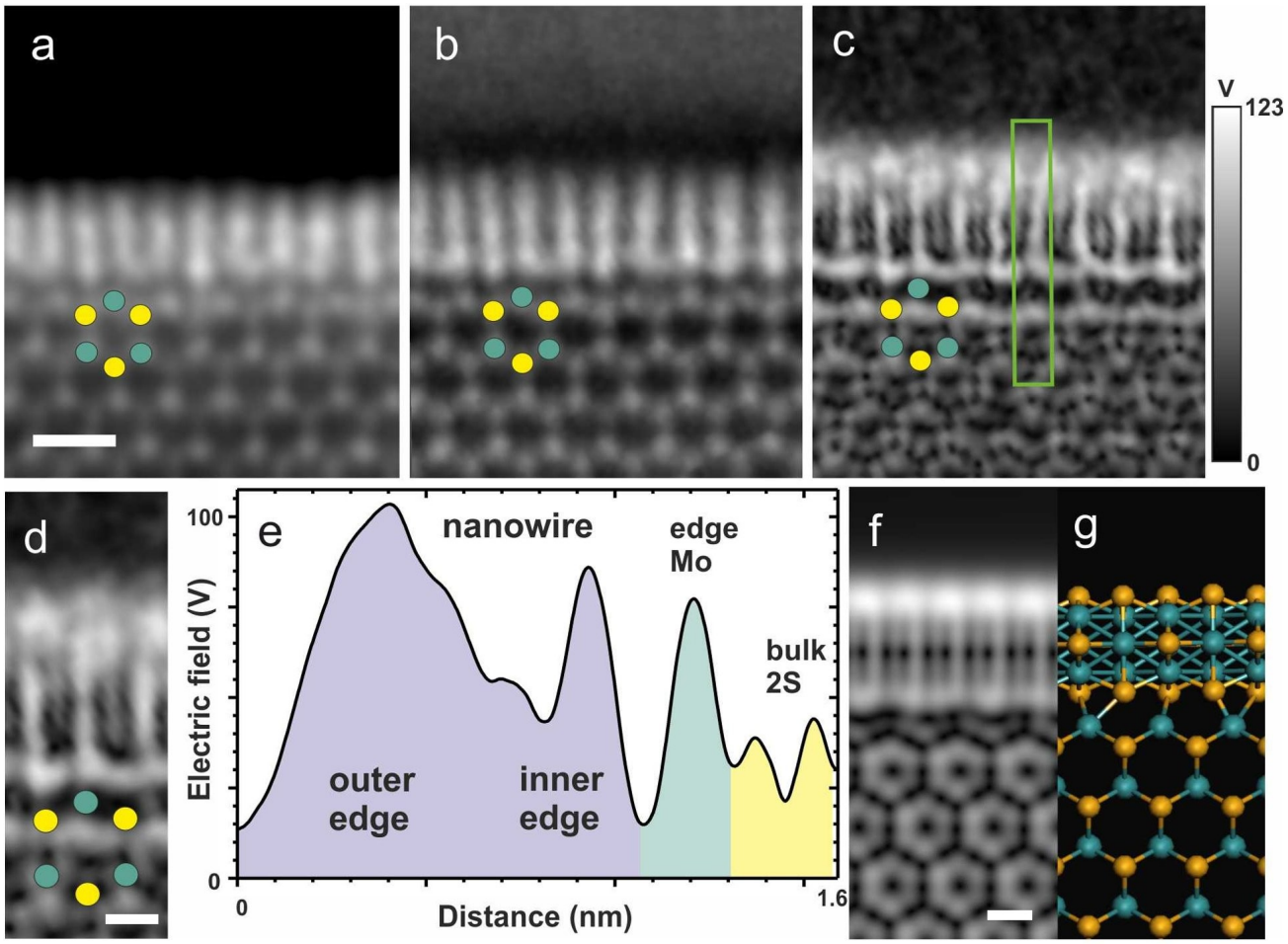

Figure 6. (a) ADF image of a nanowire attached to Mo zz edge. Scale bar in panel a indicates 0.5 nm and applies to panels b and c. (b) Reconstructed phase and (c) corresponding $|E_{\perp}|$ map. (d) Enlarged image of panel c. Scale bar indicates 0.2nm. (e) Intensity line profile box-indicated lengths (starting from 1 to 2) in panel c, color coded for different atoms. (f) Reconstructed $|E_{\perp}|$ map from simulated 4D-STEM data using the atomic model in (g). Scale bar indicates 0.2nm.

To fully understand the contrast formation mechanisms in the electric field reconstructions from 4D-STEM in atomic models with edges we performed both coherent simulations and those containing partial coherency by considering source size effects and chromatic spread in the electron source, see

supplementary methods for details. Fully coherent multislice image simulations of the Mo zz edge with a 1S edge decoration (model in figure 2h), figure S11, show that the outermost 1S atom and Mo atom do not have increased electric field strength, when using an independent atom model as the potential, but do show the increase in the electric field distance, as postulated in figure 1b. This indicates that an increase in the edge tail gives rise to new electric field distributions at the edge, and then the local bonding coordination dictates the oscillation patterns in 1D. The DFT calculated electric field, figure S12, also shows the same elongation in the electric field decay at the edge, and also shows no signs of significant increase in magnitude, with the comparison of the two in figure S13 showing the edge electric fields have similar spatial distributions. This is different to the experimental observations in figure 2, where a slight increase in electric field magnitude is observed in the 4D-STEM reconstructions, and supported by the multislice image simulations that include partial coherencies, figure 2g. Figure S13 shows that when you increase the source size, but neglect chromatic spread, the end result is that the spatial resolution reduces, but the magnitude of the electric field at the edge increases relative to the central area. However, the spatial features of the edge electric field distributions are retained and just broadened. Figure S14 shows that including chromatic spread into the simulations causes a further increase in the edge electric field magnitude relative to the bulk, but again the qualitative spatial distribution is retained. Partial coherency from chromatic spread is introduced using the established approach of weighting various defocus values to the overall 4D-STEM data set. Figure S15 shows the CoM images for various defocus values. The reason for the increase in the edge electric field intensity relative to the bulk in these simulations is due to the effect of area sampling on the transfer of contrast to the final CoM data. When sampling a small area, i.e coherent conditions, all frequencies are transferred appropriately to the CoM intensity

and the result replicates the DFT predictions. When the electron probes a larger area, then contributions from the edge region are transferred to the CoM, while lower frequencies are not. For example, a large electron probe (i.e 1nm) experiences a uniform electric field in the central bulk area of MoS_2, when scanning across the region and the CoM deflection is negligible. But when this large probe transitions across the edge region the electric field, change is detected and CoM deflection occurs. Therefore, the transfer of contrast to the CoM for different spatial features depends on the probe size. While this is not a traditional contrast transfer function, the result is that probe-size influences the spatial frequency dependence of contrast transfer to the CoM data that leads to edges always having a higher intensity than the bulk regions. This phenomenon is also going to occur for defects and other features that have spatial size larger than the lattice spacings. However, we show that if the defocus of the sample is small, and the chromatic spread and source size are accounted for, the multlislice image simulations match the qualitative spatial distributions of the electric field at the edges, but may slightly overestimate their magnitude. Further work is needed to explore quantitative 4D-STEM imaging of electric fields to account for valance charge redistributions, but that is beyond this current work.

Conclusions

4D-STEM was used to reconstruct electric field maps at the edge regions of 2D MoS_2 crystals and revealed the presence of 1D edge states with oscillations in intensity. The in-situ heating created long uniform edges that enabled the periodic electric field patterns to be visualized by 4D-STEM. These electric field oscillations at the edge provide insights into locations for adatom adsorption. Light elements were also detected, most likely S atoms, in both the electric field images and the

iDPC reconstructions, which were nearly invisible in the HAADF-STEM images. This shows the importance of using multiple modes of contrast in imaging structure to obtain both light and heavy elements all together, where HAADF-STEM imaging alone can miss out on the lighter elements. DFT indicated that edges can have increased magnitude of electric field, with the intrinsic mechanism responsible being the reduced electric field screening felt at the outermost edge due to the absence of other atoms. Such edge enhancements were observed in the experimental data of electric field. These results demonstrate that the incident electron beam is highly sensitive to changes in the local electrostatic screening arising from both nearest neighbour atoms and also the electron cloud around individual atoms. Our results also showcase how 4D-STEM can visualize contrast features that are not detected using conventional ADF-STEM imaging.

Methods

MoS_2 was grown by direct sulphurization using a double tube method previously reported.[31] The soda lime glass substrate was first cleaned in deionized water, acetone and isopropanol, and MoO_3 powder precursor (20 mg, 99.5%, Sigma-Aldrich) dissolved in 28.0% NH_4OH solution was spin-coated onto the glass substrate. The substrate was then heated at 300 °C in air to remove residual water. For sulphurization, the sulphur powder (300 mg, 99.5%, Sigma-Aldrich) and the substrate were sealed in a quartz tube and flushed with 500 sccm argon for 30 minutes to purge and then 150 sccm for growth. The MoO_3/glass downstream was first heated to 800 °C, and the sulphur upstream was heated to 180 °C in a separate furnace followed by subsequent growth for 5 minutes. Finally, the tube was removed from the furnace for fast cooling. To transfer the MoS_2 to TEM grids, the MoS_2/glass was first spin coated with PMMA, baked on a hotplate at 150 °C for 5 minutes and then slowly immersed in deionised water to detach the PMMA/MoS_2 thin film from the glass. The film

was then transferred onto a DENS heating chip and dried in an ambient environment overnight. To enhance adhesion between the heating chip and the materials, they were annealed at 180 °C for 30 minutes. The samples were then immersed in acetone for 24 hours and isopropanol for 10 minutes to remove all the PMMA. To ensure cleanliness of the final specimen, the chip was heated to ~ 700 °C during acquisition (to stop beam-induced contamination) using a single tilt DENS Solution heating holder. The 4D STEM data were recorded using a JEM ARM300CF with a Merlin Medipix high speed pixelated direct electron detector, operating at an accelerating voltage of 60kV.

Acknowledgement

Y.W. thanks support from China Scholarship Council. S.F. and E.K. were both supported by the STC Center for Integrated Quantum Materials, NSF Grant No. DMR-1231319. We thank Diamond Light Source for access and support in use of the electron Physical Science Imaging Centre (Instrument E02 and proposal number EM**20345**) that contributed to the results presented here. Work at the Molecular Foundry was supported by the Office of Science, Office of Basic Energy Sciences, of the U.S. Department of Energy under Contract No. DE-AC02-05CH11231.

Supporting Information

4D-STEM experimental acquisition details. 4D-STEM Reconstruction Details. Multislice image simulation details. Density functional theory details. ADF-STEM images of MoS_2 edges. 4D-STEM and ADF-STEM images of Mo reconstructed zigzag edges. Electric field vector map of MoS_2 edge. Time-series of ADF-STEM images showing MoS nanowires forming at MoS_2 edges.

References

1. Bollinger, M. V., Lauritsen, J. V., Jacobsen, K. W., Norskov, J. K., Helveg, S., Besenbacher, F., One-Dimensional Metallic Edge States in MoS_2. *Phys. Rev. Lett.* **87**, 196803 (2001).

2. Li, Y., Wang, H., Xie, L., Liang, Y., Hong, G., Dai, H., MoS_2 Nanoparticles Grown on Graphene: An Advanced Catalyst for the Hydrogen Evolution Reaction. *J. Am. Chem. Soc.* **133**, 7296–7299 (2011).

3. Jaramillo, T. F., Jorgensen, K. P., Bonde, J., Nielsen, J. H., Horch, S., Chorkendorff, I., Identification of Active Edge Sites for Electrochemical H_2 Evolution from MoS_2 Nanocatalysts. *Science* **317**, 100–102 (2007).

4. Lukowski, M. A., Daniel, A. S., Meng, F., Forticaux, A., Li, L., Jin, S., Enhanced Hydrogen Evolution Catalysis from Chemically Exfoliated Metallic MoS_2 Nanosheets. *J. Am. Chem. Soc.* **135**, 10274–10277 (2013).

5. Yin, X., Ye, Z., Chenet, D. A., Ye, Y., O'Brien, K., Hone, J. C., Zhang, X., Edge Nonlinear Optics on a MoS_2 Atomic Monolayer. *Science* **344**, 488–490 (2014).

6. Gutiérrez, H. R., Perea-Lopez, Elias, A. L., Berkdemir, A., Wang, B., Lv, R., Lopez-Urias, F., Crespi, V. H., Terrones, H., Terrones, M., Extraordinary Room-Temperature Photoluminescence in Triangular WS_2 Monolayers. *Nano Lett.* **13**, 3447–3454 (2013).

7. Nan, H., Wang, Z., Wang, W., Liang, Z., Lu, Y., Chen, Q., He, D., Tan, P., Miao, F., Wang, X., Wang, J., Ni, Z., Strong Photoluminescence Enhancement of MoS_2 Through Defect Engineering and Oxygen Bonding. *ACS Nano* **8**, 5738–5745 (2014).

8. Lin, K. I., Ho, Y-H., Liu, S-B., Ciou, J-J., Huang, B-T., Chen, C., Chang, H-C., Tu, C-L., Chen, C-H., Atom-Dependent Edge-Enhanced Second-Harmonic Generation on MoS_2 Monolayers. *Nano Lett.* **18**, 793–797 (2018).

9. Bruix, A., Fuchtbauer, H. G., Tuxen, A. K., Walton, A. S., Andersen, M., Porsgaard, S., Besenbacher, F., Hammer, B., Lauritsen, J., In Situ Detection of Active Edge Sites in Single-Layer MoS_2 Catalysts. *ACS Nano* **9**, 9322–9330 (2015).

10. Lin, J., Cretu, O., Zhou, W., Suenaga, K., Prasai, D., Bolotin, K., Cuong, N. T., Otani, M., Okada, S., Lupini, A. R., Idrobo, J-C., Caudel, D., Burger, A., Ghimire, N. J., Yan, J., Mandrus, D. G.,

Pennycook, S. J., Pantelides, S. T., Flexible Metallic Nanowires with Self-Adaptive Contacts to Semiconducting Transition-Metal Dichalcogenide Monolayers. *Nat. Nanotechnol.* **9**, 436–442 (2014).

11. Warner, J. H., Lin, Y. C., He, K., Koshino, M., Suenaga, K. Atomic Level Spatial Variations of Energy States along Graphene Edges. *Nano Lett.* **14**, 6155–6159 (2014).

12. Warner, J. H., Liu, Z., He, K., Robertson, A. W., Suenaga, K. Sensitivity of Graphene Edge States to Surface Adatom Interactions. *Nano Lett.* **13**, 4820–4826 (2013).

13. Suenaga, K. & Koshino, M., Atom-by-atom Spectroscopy at Graphene Edge. *Nature* **468**, 1088–1090 (2010).

14. Fang, S., Wen, Y., Allen, C. S., Ophus, C., Han, G. G. D., Kirkland, A. I., Kaxiras, E., Warner, J. H., Atomic Electrostatic Maps of 1D Channels in 2D Semiconductors using 4D Scanning Transmission Electron Microscopy. *Nat. Commun.* **10**, 1127 (2019).

15. Caswell, T. A., Ercius, P., Tate, M. W., Ercan, A., Gruner, S. M., Muller, D. A., A High-Speed Area Detector for Novel Imaging Techniques in a Scanning Transmission Electron Microscope. *Ultramicroscopy* **109**, 304–311 (2009).

16. Shibata N., Findlay, S. D., Matsumoto, T., Kohno, Y., Seki, T., Sanchez-Santolino, G., Ikuhara, Y., Direct Visualization of Local Electromagnetic Field Structures by Scanning Transmission Electron Microscopy. *Acc. Chem. Res.* **50**, 1502−1512 (2017).

17. Tate, M. W., Purohit, P., Chamberlain, D., Nguyen, K. X., Hovden, R., Chang, C. S., Deb, P., Turgut, E., Heron, J. T., Schlom, D. G., Ralph, D. C., Fuchs, G. D., Shanks, K. S., Philipp, H. T., Muller, D. A., Gruner, S. M., High Dynamic Range Pixel Array Detector for Scanning Transmission Electron Microscopy. *Microsc. Microanal.* **22**, 237–249 (2016).

18. Müller, K., Krause, F. F., Beche, A., Schowalter, M., Galioit, V., Loffler, S., Verbeek, J., Zweck, J., Schattschneider, P., Rosenauer, A., Atomic Electric Fields Revealed by a Quantum Mechanical Approach to Electron Picodiffraction. *Nat. Commun.* **5**, 5653 (2014).

19. Müller-Caspary, K., Krause, F. F., Grieb, T., Loffler, S., Schowalter, M., Beche, A., Galioit, V., Marquardt, D., Zweck, J., Schattschneider, P., Verbeeck, J., Rosenauer, A., Measurement of Atomic Electric Fields and Charge Densities from Average Momentum Transfers using Scanning Transmission Electron Microscopy. *Ultramicroscopy* **178**, 62–80 (2017).

20. Hachtel, J. A., Idrobo, J. C., Chi, M. Sub-Ångstrom Electric Field Measurements on a Universal Detector in a Scanning Transmission Electron Microscope. *Adv. Struct. Chem. Imag.* **4**, 10 (2018).

21. Gao, W., Addiego, C., Wang, H., Yan, X., Hou, Y., Ji, D., Heikes, C., Zhang, Y., Li, L., Huyan, H., Blum, T., Aoki, T., Nie, Y., Schlom, D. G., Wu, R., Pan, X., Real-Space Charge-Density Imaging with Sub-Angström Resolution by Four-Dimensional Electron Microscopy. *Nature* **575**, 480–484 (2019).

22. Ishikawa, R., Findlay, S. D., Seki, T., Sanchez-Santolino, G., Kohno, Y., Ikuhara, Y., Shibata, N., Direct Electric Field Imaging of Graphene Defects. *Nat. Commun.* **9**, 3878 (2018).

23. Müller-Caspary, K., Duchamp, M., Rosner, M., Migunov, V., Winkler, F., Yang, H., Huth, M., Ritz, R., Simson, M., Ihle, S., Soltau, H., Whling, T., Dunin-Borkowski, R., Van Aert, S., Rosenauer, A., Atomic-Scale Quantification of Charge Densities in Two-Dimensional Materials. *Phys. Rev. B* **98**, 121408 (2018).

24. Calderon, S. Ferreira, R. V., Taneja, D., Jayanth, R. T., Zhou, L., Ribeiro, R. M., Akinwande, D., Ferreira, P. J., Atomic Electrostatic Maps of Point Defects in MoS_2, Nano Letters, 21, 10157-10164, (2021)

25. de Graaf, S., Ahmadi, M., Lazic, I., Bosch, E. G. T., Kooi, B. J., Imaging Atomic Motion of Light Elements in 2D Materials with 30 kV Electron Microscopy, Nanoscale, 13, 20683, (2021).

26. Chen, Q., Li, H., Xu, W., Wang, S., Sawada, H., Allen, C. S., Kirkland, A. I., Grossman, J. C., Warner, J. H., Atomically Flat Zigzag Edges in Monolayer MoS_2 by Thermal Annealing. *Nano Lett.* **17**, 5502−5507 (2017).

27. Wen, Y., Ophus, C., Allen, C. S., Fang, S., Chen, J., Kaxiras, E., Kirkland, A. I., Warner, J. H., Simultaneous Identification of Low and High Atomic Number Atoms in Monolayer 2D Materials Using 4D Scanning Transmission Electron Microscopy, 19, 6482-6491 (2019)

28. Hansen, L. P. et al. Atomic-scale edge structures on industrial-style MoS_2 nanocatalysts. *Angew. Chemie. Int. Ed.* **50**, 10153–10156 (2011).

29. Schweiger, H., Raybaud, P., Kresse, G., Toulhoat, H., Shape and Edge Sites Modifications of MoS_2 Catalytic Nanoparticles Induced by Working Conditions: A Theoretical Study. *J. Catal.* **207**, 76–87 (2002).

30. Xu, H., Liu, S., Ding, Z., Tan, S. J. R., Yam, K., M., Bao, Y., Nai, C. T., Ng, M-F., Lu, J., Zhang, C., Loh, K. P., Oscillating Edge States in One-Dimensional MoS_2 Nanowires. *Nat. Commun.* **7**, 12904 (2016).

31. Xu, H., Ding, Z., Nai, C. T., Bao, Y., Cheng, F., Tan, S. J. R., Loh, K. P., Controllable Synthesis of 2D and 1D MoS_2 Nanostructures on Au Surface. *Adv. Funct. Mater*. **27**, 1603887 (2017).

32. Li, S., Lin, Y-C., Zhao, W., Wu, J., Wang, Z., Hu, Z., Shen, Y., Tang, D-M., Wang, J., Zhang, Q., Zhu, H., Chu, L., Zhao, W., Liu, C., Sun, Z., Taniguchi, T., Osada, M., Chen, W., Xu, Q-H., Wee, A. T. S., Suenaga, K., Ding, F., Eda, G., Vapour–Liquid–Solid Growth of Monolayer MoS_2 Nanoribbons. *Nat. Mater*. **17**, 535-542 (2018).

33. Koh, A. L., Wang, S., Ataca, C., Grossman, J. C., Sinclair, R., Torsional Deformations in Subnanometer MoS Interconnecting Wires. *Nano Lett.* **16**, 1210–1217 (2016).

34. Oxley, M. P.; Dyck, O. E. The Importance of Temporal and Spatial Incoherence in Quantitative Interpretation of 4d-Stem. *Ultramicroscopy*, 215, 113015, (2020).

35. Lu, Y., Chen, T., Ryu, G. H., Huang, H., Sheng, Y., Chang, R-J., Warner, J. H., Self-Limiting Growth of High Quality 2D Monolayer MoS2 by Direct Sulfurization Using Precursor-Soluble Substrates for Advanced Field-Effect Transistors and Photodetectors. *ACS Appl. Nano. Mater.* 2, 369-378 (2019)

TOC graphic